On the Relationship between Regional Ocean Heat Content and Sea Surface Height

JOHN T. FASULLO AND PETER R. GENT

National Center for Atmospheric Research, Boulder, Colorado

(Manuscript received 30 December 2016, in final form 7 August 2017)

ABSTRACT

An accurate diagnosis of ocean heat content (OHC) is essential for interpreting climate variability and change, as evidenced for example by the broad range of hypotheses that exists for explaining the recent hiatus in global mean surface warming. Potential insights are explored here by examining relationships between OHC and sea surface height (SSH) in observations and two recently available large ensembles of climate model simulations from the mid-twentieth century to 2100. It is found that in decadal-length observations and a model control simulation with constant forcing, strong ties between OHC and SSH exist, with little temporal or spatial complexity. Agreement is particularly strong on monthly to interannual time scales. In contrast, in forced transient warming simulations, important dependencies in the relationship exist as a function of region and time scale. Near Antarctica, low-frequency SSH variability is driven mainly by changes in the circumpolar current associated with intensified surface winds, leading to correlations between OHC and SSH that are weak and sometimes negative. In subtropical regions, and near other coastal boundaries, negative correlations are also evident on long time scales and are associated with the accumulated effects of changes in the water cycle and ocean dynamics that underlie complexity in the OHC relationship to SSH. Low-frequency variability in observations is found to exhibit similar negative correlations. Combined with altimeter data, these results provide evidence that SSH increases in the Indian and western Pacific Oceans during the hiatus are suggestive of substantial OHC increases. Methods for developing the applicability of altimetry as a constraint on OHC more generally are also discussed.

1. Introduction

Understanding the energy flows through the climate system is imperative for interpreting climate variability and change in the context of the observational record (Trenberth et al. 2009). Changes in these flows can have profound effects on global surface temperature and perceptions of climate change. However, the interpretation of observed variability, such as for example during the recent so-called hiatus in global warming (Trenberth and Fasullo 2013), depends critically on our ability to monitor in space and time ocean heat content (OHC) and associated surface fluxes and heat transports (Meehl et al. 2011; England et al. 2014).

While adequate sampling of the upper ocean on a global scale began in the mid-2000s (Roemmich and Gilson 2009), regional and seasonal variability remains a challenge to diagnose (Trenberth et al. 2016). Moreover, large and important ocean regions, such as the deep ocean below 2 km, polar oceans, and marginal seas, are inadequately observed even in the present day (Durack et al. 2014). In contrast, radar altimetry has provided stable, near-global, well-calibrated, and densely sampled observations of sea surface height (SSH) since late 1992 (Nerem et al. 2010). In early work, White and Tai (1995) relate TOPEX SSH observations over 1993–94 to OHC variability diagnosed from XBT observations and find strong positive regressions over 30°S–60°N. Chambers et al. (1998) compare TOPEX SSH data to OHC observations from the TOGA–TAO array in the tropical Pacific Ocean over 1993–96 and again find positive regressions between these two estimates.

However, Sato et al. (2000) point out the need for salinity measurements in order to correctly estimate OHC from TOPEX SSH observations because of the salinity effect on density. Jayne et al. (2003) show how satellite observations of the gravity field can be related to ocean bottom pressure, which can be used to reduce errors in estimating OHC from SSH caused by barotropic variability at high latitudes. They conclude that this technique works well over the annual cycle, but problems arise trying to estimate changes in OHC from

Corresponding author: John T. Fasullo, fasullo@ucar.edu

DOI: 10.1175/JCLI-D-16-0920.1

SSH over longer time scales. The importance of changes to the wind-driven ocean circulation in influencing SSH variability was also emphasized by analysis of observations in Guinehut et al. (2006) and Suzuki and Ishii (2011). Recently, Forget and Ponte (2015) compare SSH observations with the output from the ECCO global state estimation. In a very thorough analysis, they show that on long time scales both wind stress and salinity variability, in addition to OHC variability, are important in causing SSH variability at many locations across the global oceans. A number of factors can therefore obscure, and at times overwhelm, the simple expected positive relationship between OHC and SSH over long time scales (Pardaens et al. 2011). The relative influence of internal versus forced variability on the relationship is also not well understood. Therefore, the extent to which a quantitative diagnosis of OHC, and by extension associated transports and fluxes, can be inferred from this SSH record as a function of time scale and region remains unclear.

Over 90% of the additional heat in the climate system due to increased levels of greenhouse gases goes into increasing OHC (IPCC 2013). Our ability to estimate OHC has dramatically improved since the mid-2000s, largely because of the enhanced sampling of the ocean by Argo floats that currently record temperature from the surface to 2-km depth. These data have also been used in the development of ocean reanalysis products since that time, although products that assimilate SSH data reach back to the start of the satellite altimeter era in late 1992. For example, Fig. 1a shows decadal changes in AVISO SSH between the 2004–13 and 1993–2003 periods, after the global mean has been removed. Altimeter data have been assimilated into the Ocean Reanalysis Pilot 5 (ORAP5) product (Zuo et al. 2015), and the change in the reanalysis SSH between the same periods is shown in Fig. 1b. The two figures are very similar, with a spatial correlation of 0.67, which indicates that ORAP5 is strongly constrained to follow the altimeter data on decadal time scales. Figure 1c shows the corresponding change in the ORAP5 OHC integrated from the surface to 2 km, also with the global mean removed. Comparison of Figs. 1b and 1c shows that all of the regions of large SSH increase, such as the Indian, tropical western Pacific, and subpolar North Atlantic Oceans, are reflected in large positive increases in OHC, as is expected. In the zonal mean, disproportionate increases in both SSH and OHC are also evident in the south equatorial Indian Ocean (0°–30°S), Southern Ocean (35°–50°S), and northern Atlantic Ocean (40°–65°N). Similarly, regions where SSH fell, most notably in the eastern tropical Pacific and midlatitude North Atlantic (~40°N) Oceans, are characterized by OHC decreases, and in the zonal mean the tropical Pacific Ocean is generally characterized by weak warming and modest SSH increases. However, there are significant regions of the oceans where OHC and SSH diverge, with ORAP5 indicating a reduction in OHC while AVISO and ORAP5 show increases in the full SSH field. This is especially true in the southeast Pacific, high-latitude Southern, western subtropical Pacific, subtropical North Atlantic, and south Indian Oceans. If these observations and ocean reanalysis are correct, they indicate regions where factors other than OHC are significantly affecting changes in SSH. Such factors may include changes in ocean dynamics and circulation and changes in salinity arising, for example, from the surface water balance and freshwater inputs from rivers and melting ice. In nature, additional factors omitted from ORAP5 can also influence regional SSH, including the isostatic rebound of Earth and gravitational influences arising from variations in ice sheet mass balance and terrestrial water storage. However, their contributions to the differences in Fig. 1 are likely to be small (Mitrovica et al. 2001).

One way to study the effects of changing salinity and ocean circulation on SSH is to use climate models, such as the Community Earth System Model (CESM; Meehl et al. 2013) and the Geophysical Fluid Dynamics Laboratory (GFDL)-ESM2M model (Dunne et al. 2012). Large ensembles (LE) of at least 30 members of simulations from the mid-twentieth century to 2100 have recently been produced for both the CESM (Kay et al. 2015) and GFDL (Rodgers et al. 2015) models, and these help characterize the influence of internal variability on SSH and OHC fields over brief periods such as the altimeter era. These LE also provide a unique opportunity to estimate the forced climate response in the absence of model structural and forcing differences. The ensembles will be used to document regressions of OHC against SSH on high-frequency, annual, and low-frequency time scales. Comparing the two models will show what results are consistent between them and so will be considered more reliable. It is notable that both models consistently score among the most skillful models in depicting present-day climate (Knutti et al. 2013).

A number of scientific questions will be addressed. Can the AVISO and ORAP5 data be used to validate the SSH and OHC relationships derived from the models? In the models, on what time scales and in which regions does SSH variability reflect OHC variability in both control and forced runs, and where and on what time scales do SSH and OHC diverge? What circumstances and which physical processes are involved in their divergence? Is there evidence for such a divergence in observations? The outline of the paper is as follows: Section 2 briefly documents the observations and models used, and the models are validated against

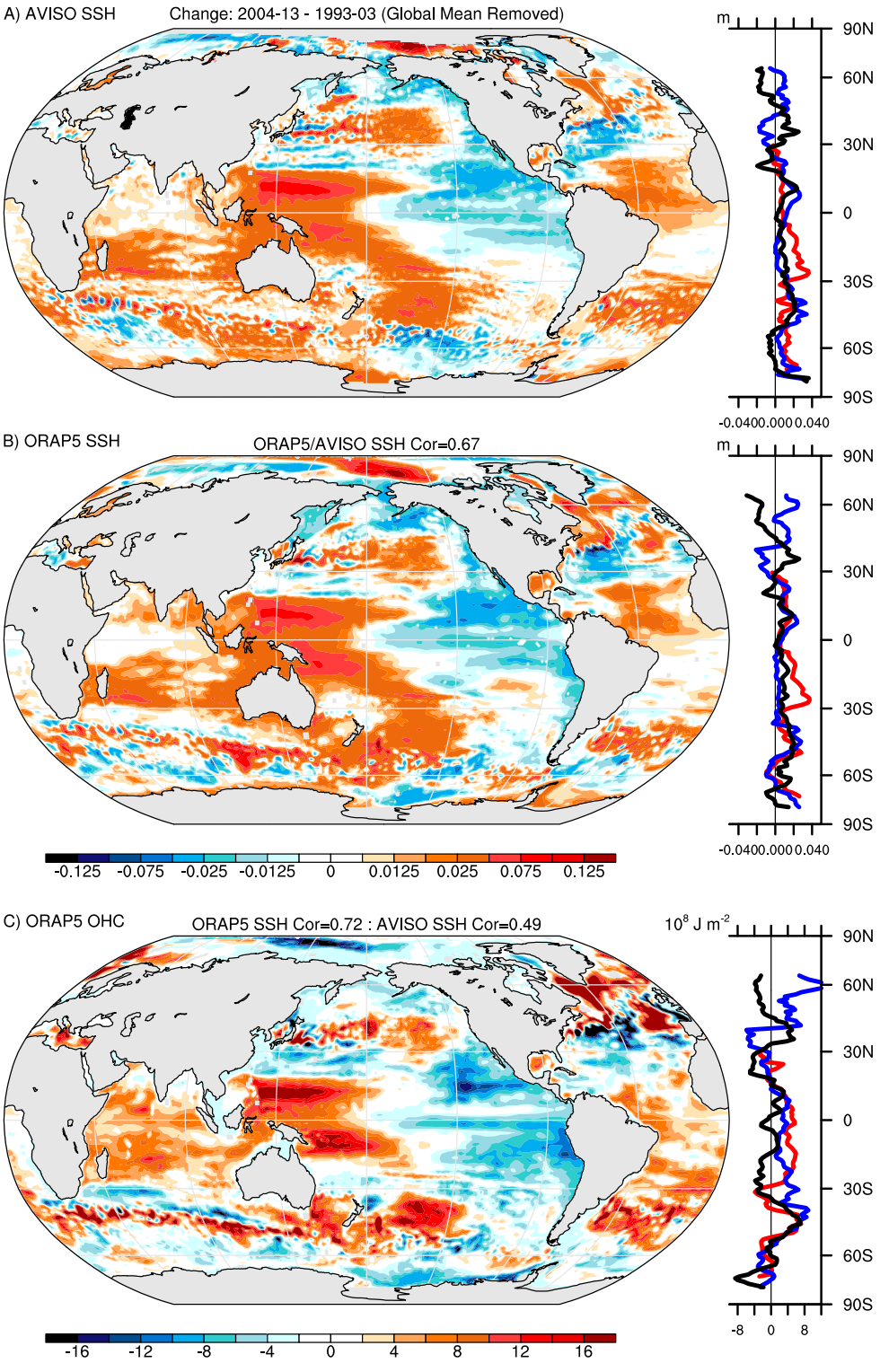

FIG. 1. Decadal differences in (a) AVISO and (b) ORAP5 SSH (m) and (c) 0–2-km ORAP5 OHC (10^8 J) between 1993–2003 and 2004–13. Zonal means are indicated for the Pacific (black), Atlantic (blue), and Indian Ocean (red) basins.

the observations in section 3. The main results from the long model runs are presented in section 4, and section 5 contains our discussion and conclusions.

2. Observations and models

The AVISO SSH data are documented at, and available from, the AVISO website (http://www.aviso.altimetry.fr/en/my-aviso.html). It is a compilation of observations from several altimeter missions (*SARAL*, *Cryosat-2*, *Jason-1*, *Jason-2*, TOPEX/Poseidon, *Envisat*, *GFO*, *ERS-1*, *ERS-2*, and *Geosat*), allowing for near-global coverage, and starts in 1993, continuing to the present time. It spans the global ice-free ocean, with the exception of the central Arctic Ocean, and is on a 0.25° × 0.25° grid, with sufficient coverage to provide a global mean estimate every 10 days. From these retrievals, a gridded monthly product is then constructed. The ORAP5 ocean reanalysis is made at, and available from, the European Centre for Medium-Range Weather Forecasts website (http://www.ecmwf.int/en/research/climate-reanalysis/ocean-reanalysis). Various ocean observations, including temperature and salinity profiles and altimeter-derived SSH anomalies, are assimilated into a global ¼° × ¼° ocean model, providing monthly high-resolution temperature, salinity, and velocity fields on 75 levels. The reanalysis benefits from additional data beginning in late 1992 when altimetry data became available for assimilation and became even more accurate after the mid-2000s when Argo data are assimilated (Zuo et al. 2015). Even though ORAP5 is an ocean reanalysis, we will sometimes refer to it as ''observations,'' in order to distinguish it from results using climate models.

The CESM LE uses the CESM1(CAM5) version, which has a horizontal resolution of about 1° in all components except for the ocean where the grid size is variable and somewhat finer. There is a very long control run of almost 2000 yr, which is forced by constant 1850 conditions and provides ten uninterrupted 180-yr intervals, for comparison to the full LE runs, and seventy-two 25-yr intervals, for comparison with the altimeter-era data. The ensemble's 40 members span the years 1920–2100 and use observed forcings of solar radiation, greenhouse gases, stratospheric ozone, and aerosols (anthropogenic and natural including volcanic) between 1920 and 2005. After that the runs are forced by the representative concentration pathway 8.5 (RCP8.5) levels of greenhouse gases (van Vuuren et al. 2011) in which carbon dioxide levels increase from 380 ppm in 2005 to 930 ppm in 2100. This is a very strong forcing and causes large changes to Earth's climate by 2100 as described in Meehl et al. (2013) and Jahn and Holland (2013). The CESM's ocean component is the Parallel Ocean Program, version 2 (POP2; Smith et al. 2010), which is a fixed-volume ocean that does not account for global mean sea level rise but does simulate regional SSH variability associated with steric and dynamic effects.

The GFDL LE uses GFDL-ESM2M, which has a resolution of 2° in the atmosphere and land components and ~1° in the ocean and sea ice components (see Dunne et al. 2012). This ensemble has 30 members and runs from 1950 to 2100. As for the CESM LE, the forcings are based on observations up to 2005 and thereafter use the RCP8.5 forcing scenario (Rodgers et al. 2015). This model was found to be skillful in simulating surface temperature, salinity, and height patterns and tropical Pacific and Southern Ocean circulation and variability (Dunne et al. 2012). In contrast to the CESM, the GFDL-ESM2M ocean component is the Modular Ocean Model, version 4.1, which accounts for steric global changes in ocean volume but not for increases in ocean mass. However, in order to compare with CESM results, this globally averaged steric change in SSH was subtracted from each of the monthly GFDL-ESM2M datasets. In addition, for consistency the globally averaged component was removed from both the AVISO SSH data and the ORAP5 OHC data before computing OHC–SSH regressions, thus eliminating both changes in ocean mass and the global steric component that are not in the CESM results.

Four time-filtering conventions have been applied to the monthly SSH and OHC time series prior to computing local regressions and correlations. Prior to removing the climatological mean these filters retain 1) all time scales (ALL), 2) the monthly climatological annual cycle (AC), 3) high frequencies (HIGH), which include frequencies up to a few years (e.g., ENSO), and 4) low frequencies (LOW), which retain low-frequency variability and long-term climate change signals. The HIGH filter removes variability estimated from a 5-yr smoother [adapted from the decadal smoother called the second filter in appendix 3A of Trenberth et al. (2007)], and the LOW filter removes the frequencies retained in the HIGH filter so that the LOW and HIGH time series added together sum to the annual mean of the ALL time series. An example of time series from a 2° × 2° area centered at 15°N, 60°W in the North Atlantic in a CESM run is shown in Fig. 2. Figure 2a shows the SSH and OHC time series that contain ALL time scales, while Figs. 2b, 2c, and 2d show the AC, HIGH, and LOW, filtering respectively. Note that all filters remove the annual mean value so that averages over the records are zero. HIGH filtering eliminates any trends and decadal variability, while LOW filtering clearly shows the trends and decadal variability. This region was chosen because it

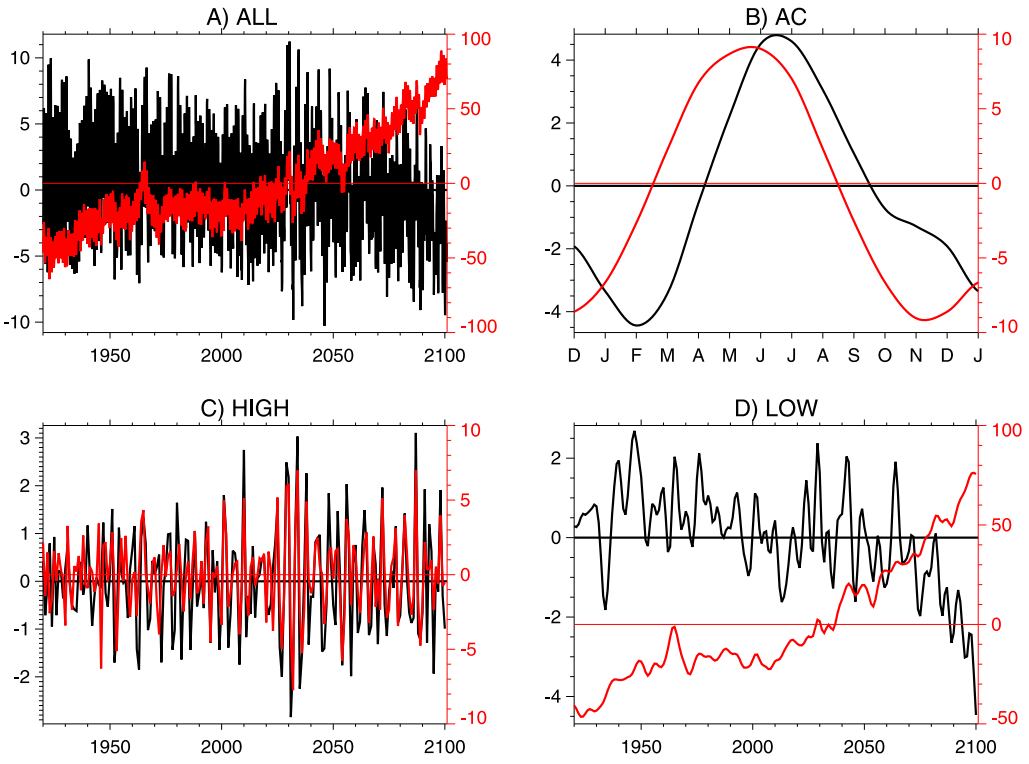

FIG. 2. Time-filtering conventions applied to SSH (black; cm) and OHC anomalies (red; 10^8 J m^{-2}) at 15°N, 60°W prior to computing the regressions for (a) ALL, (b) AC, (c) HIGH, and (d) LOW time-scale filtering.

shows opposite trends over 2050–2100, with the SSH decreasing while the OHC is increasing. In addition, the ensemble regressions shown later are an average of the regression fields calculated from each of the individual ensemble members, after the model data have been spectrally truncated to include wavenumbers 63 and lower.

3. Climate model validation

Figure 3 shows the ALL, AC, HIGH, and LOW regressions between AVISO SSH and ORAP5 OHC over 1993–2015, and Fig. 4 shows the same plots using SSH and OHC from the CESM LE. Note that the stippled areas in these figures indicate regions where OHC explains less than half the variance in SSH. This occurs in the Arctic and Southern Oceans and in regions of both the North and South Atlantic. There is much less stippling in the Pacific and Indian Oceans where OHC generally explains more than half the SSH variance. Comparison of Figs. 3a and 4a shows that when all frequencies are retained there is rather good agreement between the global mean modeled ($r = 1.52 \times 10^7$ J m^{-2} mm^{-1}) and observed ($r = 1.32 \times 10^7$ J m^{-2} mm^{-1}) values. Both regressions are positive virtually everywhere, and the locations of the highest regressions are in the subpolar North Atlantic and in the region of the Antarctic Circumpolar Current (ACC), especially south of Australia. In addition, both have very weak regressions around Antarctica and in the Arctic Ocean, in part because salinity changes dominate seawater density changes at colder temperatures. Agreement is not as good over the annual cycle (Figs. 3b and 4b) and over HIGH (Figs. 3c and 4c) and LOW frequencies (Figs. 3d and 4d), in that there is more small spatial variability in the observations than in the CESM. Nonetheless, the patterns do agree in the locations of the highest regressions (the North Atlantic and Southern Oceans) and in the general magnitude of the regressions with global mean CESM regressions for the AC, HIGH, and LOW filtering of 1.49, 1.63, and 1.64 $\times 10^7$ J m^{-2} mm^{-1}, respectively, with corresponding observed regressions of 1.20, 1.25, and 1.52 $\times 10^7$ J m^{-2} mm^{-1}, respectively. The systematically higher regressions in the model may arise from model biases in the vertical advection and mixing of heat, while the smoother regressions in the CESM are probably due to the multiple ensemble members involved in the average and the coarser resolution in the ocean component, which does not resolve mesoscale eddies, compared to

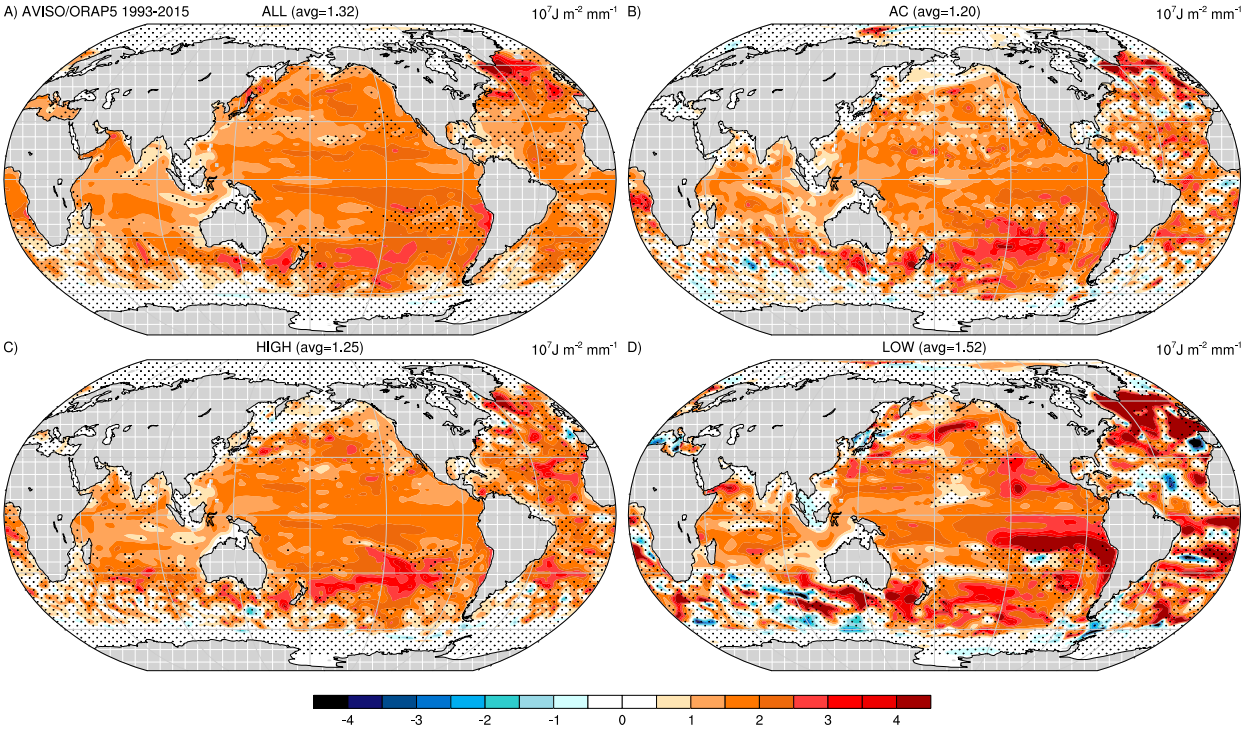

FIG. 3. Regression between AVISO SSH and ORAP5 OHC reanalysis from 1993 to 2013 for (a) ALL, (b) AC, (c) HIGH, and (d) LOW time-scale filtering. Stippling indicates regions where OHC explains less than half of the variance in SSH (i.e., $r < 0.71$).

the eddy-permitting ¼° resolution of ORAP5. Sparseness of ocean observations at depth, particularly prior to the Argo era, may also contribute to the fine structure in observed values. One notable feature of the observed low-frequency regression pattern (Fig. 3d) are the regions of negative correlations, and of particular interest is the question as to whether they are simulated by models and, if so, whether they arise from internal or forced variability; these questions will be addressed further.

Figure 5 shows the same plots as Fig. 4 but from the GFDL LE. Comparison of Figs. 3a and 5a shows that the ALL frequency regression from the GFDL LE has larger values than observed in the midlatitude North Pacific and North and South Atlantic Oceans and in the Southern Ocean. In addition, the region of negative regression near Antarctica is narrower in the GFDL LE than in the observations. These same comments apply to the GFDL AC, HIGH, and LOW time scales shown in Figs. 5b–d. The larger model low-frequency regressions compared to the AVISO/ORAP5 regressions are in regions of large variability in ocean circulation, and comparison of Figs. 3d and 5d shows they might be a little too strong in the GFDL LE. Overall, we find the agreement between the modeled and reanalysis regressions shown in Figs. 3–5 is rather good, especially the ALL and HIGH regressions. Note that there is good agreement in the stippled areas where OHC explains less than half the SSH variance. Therefore, we think that regressions derived from the much longer LE runs will provide insight into the real ocean and climate system in a range of contexts that cannot be explored using observations alone.

4. Model results

Figure 6 shows the ALL regressions between OHC and SSH from the CESM 1850 control run and LE and the GFDL LE. Again the stippled areas indicate regions where OHC explains less than half the variance in SSH. Note that the Arctic and Southern Ocean near Antarctica are stippled in the control run, but much more extensive regions of the other oceans are stippled in the forced 1920–2100 runs. Comparison of Figs. 6a and 6b shows very different regressions between the 40 strongly forced 1920–2100 runs and the 10 equal-length intervals from the 1850 control run, where all forcings are held constant. In the control run, the regressions are positive everywhere except near Antarctica and in the Arctic Ocean, where they are nearly zero. The reason for the nearly uniform regressions is that internal variability in OHC is the main contributor to long-term internal

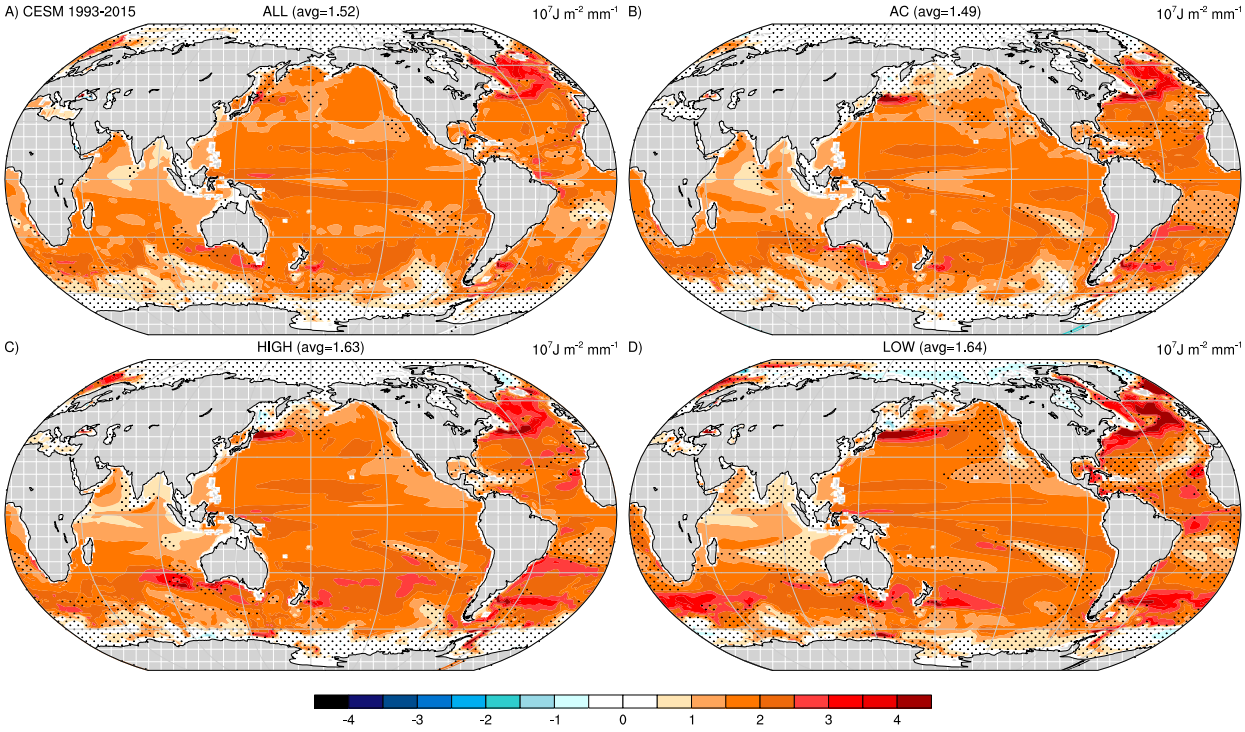

FIG. 4. As in Fig. 3, but for the CESM LE SSH and OHC from 1993 to 2015.

variability in SSH (Köhl 2014), except at very high latitudes where ocean density variations are dominated by changes in salinity rather than temperature. On shorter time scales such as the altimeter record, internal variability is found to contribute to relative minima in the SSH–OHC regression field in the Atlantic and Pacific subtropics and the Arctic and Southern Oceans (Fig. 4a). However, rarely do these result in negative regressed values equatorward of 60°.

In contrast, in the 1920–2100 runs there are large forced transient changes to the climate, which include trends in salinity and the ocean circulation due to changes in both the surface water budget and wind stress, and associated changes in advection (Vinogradova and Ponte 2013). In particular, Figs. 7a,b from the CESM and GFDL LE show positive sea surface salinity (SSS) trends in the subtropical North Atlantic, the southeast Pacific, and subtropical south Indian Oceans. In the Atlantic, these coincide with regions in which relative minima in the regressions exist between OHC and SSH (Figs. 6b,c) and to regions where negative values are evident in the LOW observed regressions (Fig. 3d). Increasing SSS in subsident subtropical regions is caused in part by an enhanced freshwater cycle in a warmer climate (Durack et al. 2012), leading to increased evaporation in these regions and, in many models, associated reductions in precipitation, leading to reductions in precipitation minus evaporation ($P - E$). Figures 7c,d show the CESM LE and GFDL LE full-depth OHC with the trend removed. They agree that more heat is taken up from the mid-twentieth century through 2100 in the Atlantic and regions of the Southern Ocean and less heat than average in the Pacific, Indian, and polar North Atlantic Oceans. There is reasonable agreement between the CESM and GFDL models on these regional patterns. In regions where the OHC trend dominates the SSH budget or where SSS trends are negatively correlated with OHC trends, regressions in Fig. 6b are generally positive, but in regions where the SSS trend dominates and is positively correlated with OHC, negative regressions often exist. In addition, ocean circulation changes can be important. The zonal wind maximum in the Southern Hemisphere has been observed to increase in strength and migrate southward over the latter part of the twentieth century (Swart and Fyfe 2012), and these changes continue in all members of the CESM and GFDL LE over the twenty-first century projections (Figs. 7e,f). These zonal wind changes drive a slightly stronger ACC, which is also displaced southward in Fig. 7e (Meijers et al. 2012), leading to an enhanced and displaced SSH gradient, causing SSH to fall near Antarctica. However, the regressions in Figs. 6b,c between OHC and SSH are positive in the Southern Ocean after the global means

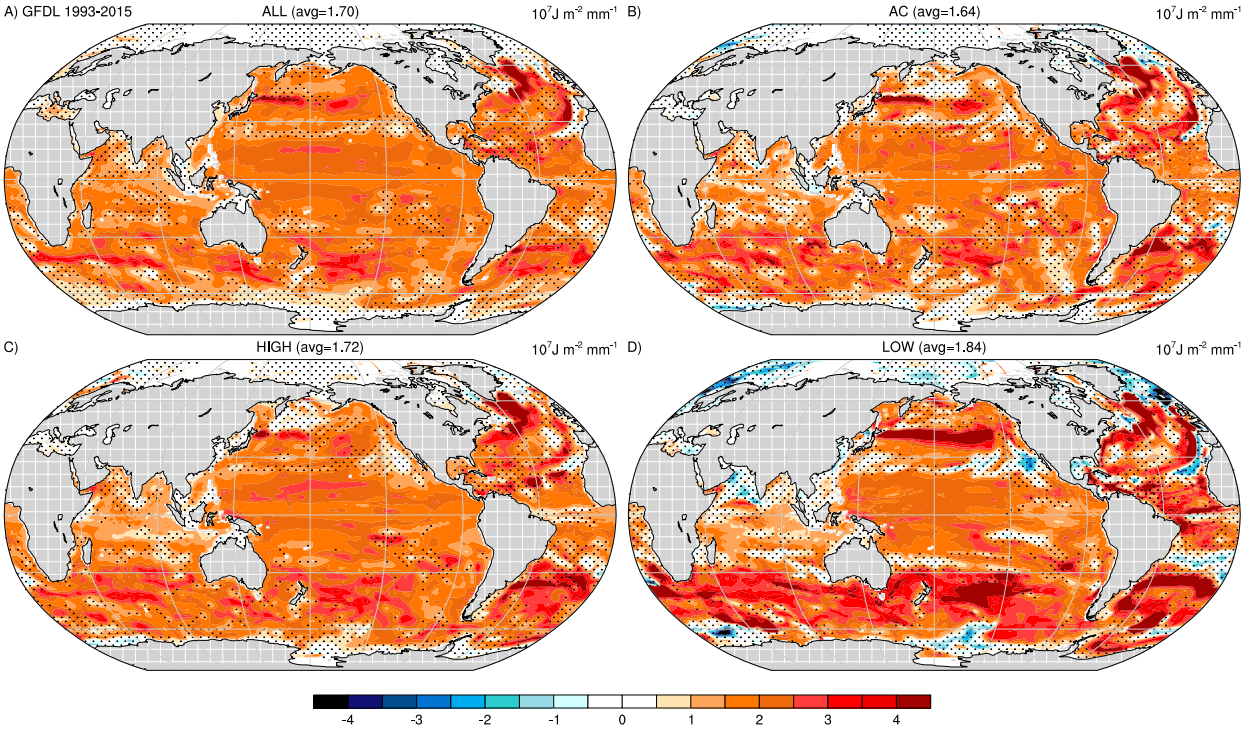

FIG. 5. As in Fig. 4, but for the GFDL LE SSH and OHC from 1993 to 2015.

have been removed because the circulation change causes dynamically consistent changes in OHC and SSH (Zhang et al. 2014). The SSH response to increased and southward-displaced Southern Hemisphere winds in an eddy-permitting ocean model is described in detail in Frankcombe et al. (2013).

Comparison of Figs. 6b and 6c shows many regions where the CESM and GFDL regressions agree but also a number of regions where they disagree. They agree on the regression sign in the large majority of the Pacific, Indian, and Southern Oceans, although there are quite large differences in the amplitudes in the North Pacific, north Indian, and Southern Oceans. The largest differences occur in the Atlantic Ocean, where the GFDL LE has a more complicated structure in the northern midlatitudes and a negative regression around 20°S compared to the CESM. The spatial character of the regression differences is closely governed by the trends in SSS and full-depth OHC shown in Fig. 7. In the CESM, the SSS trend structure is primarily that of a dipole, with a positive trend in the North Atlantic south of 45°N and a negative trend to the north, regions characterized by an increase and decrease in OHC, respectively. In the GFDL LE, there is a very strong trend in OHC in the North Atlantic tropics and subtropics (Fig. 7d) and a stronger SSS trend in the South Atlantic (Fig. 7b) compared to the CESM. These trends produce the more complicated GFDL regression pattern in the Atlantic (Fig. 6c). Both the CESM and GFDL LEs produce positive OHC–SSH regressions in the Southern Ocean and negative regressions near Antarctica. The trends in surface stresses shown in Figs. 7e,f show a dipole pattern in the Southern Ocean indicating that the ACC has shifted a little to the south in both models. However, the regressions remain positive because the global mean increase in OHC has been removed. The negative regressions near Antarctica indicate that salinity changes are influencing density more than the temperature changes in these regions of cold surface ocean.

The GFDL spatial patterns in Figs. 6c, 7b, and 7d are very similar to Figs. 9a and 10 in Yin et al. (2010), which are the steric SSH anomaly in 2091–2100 relative to 1981–2000 and the thermosteric and halosteric contributions when the GFDL CM2.1 model is forced by the A1B scenario. Note that the CM2.1 and GFDL-ESM2M models use the same ocean resolution, although the GFDL-ESM2M ocean component has several improvements compared to the CM2.1 ocean component. The study by Yin et al. (2010) contains a very thorough analysis of the spatial variability of SSH rise in twenty-first-century projections using the CM2.1. They write that weakening of the meridional overturning circulation (MOC) is responsible for the dipole pattern in the

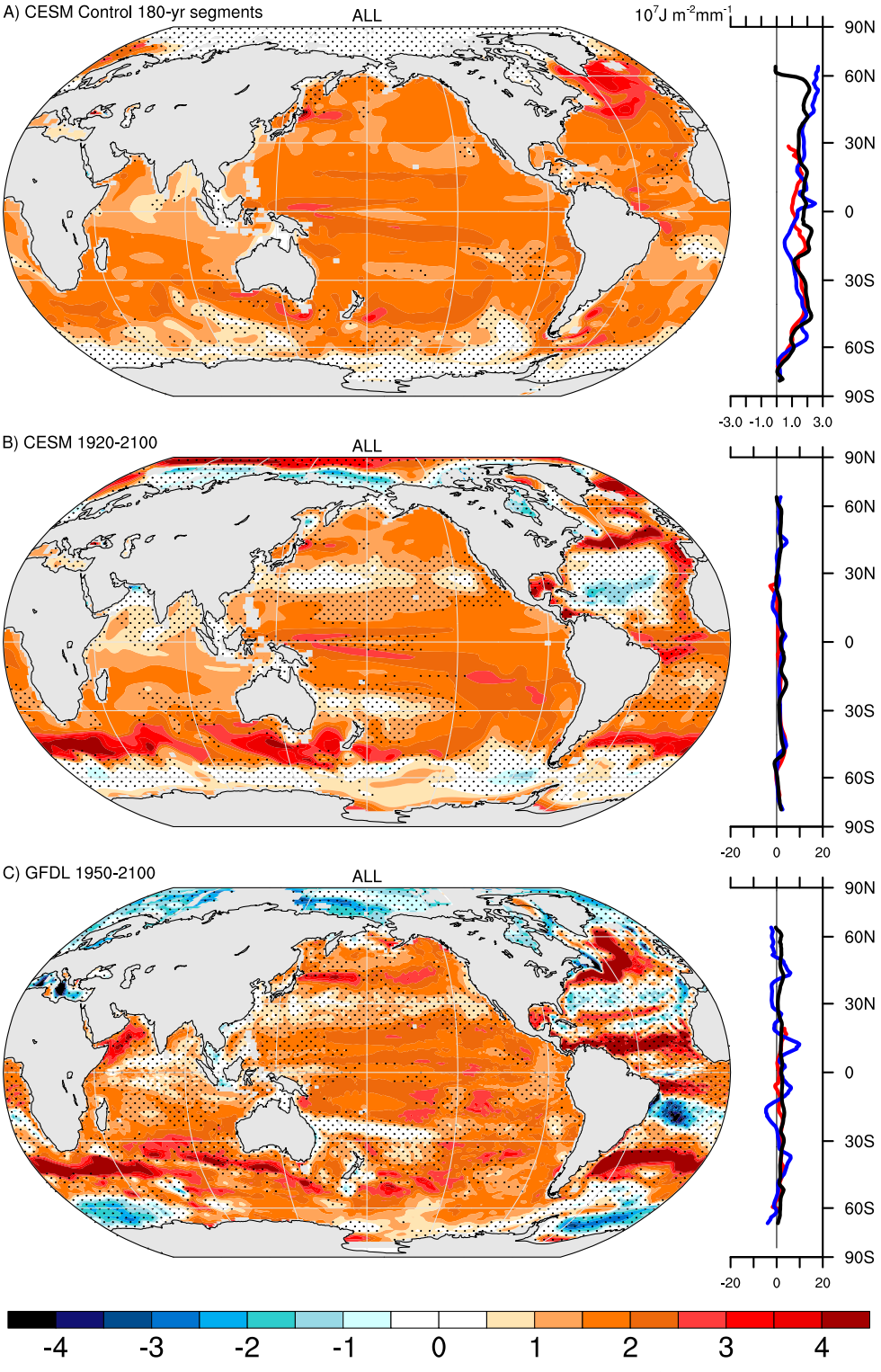

FIG. 6. Ensemble-mean regressions between OHC and SSH (10^7 J m^{-2} mm^{-1}) for ALL time scales for (a) ten 180-yr segments of the control LE simulation and from the forced (b) CESM LE runs from 1920 to 2100 and (c) GFDL LE runs from 1950 to 2100. Zonal means are indicated for the Pacific (black), Atlantic (blue), and Indian Ocean (red) basins. Stippling indicates regions where OHC explains less than half of the variance in SSH (i.e., $r < 0.71$).

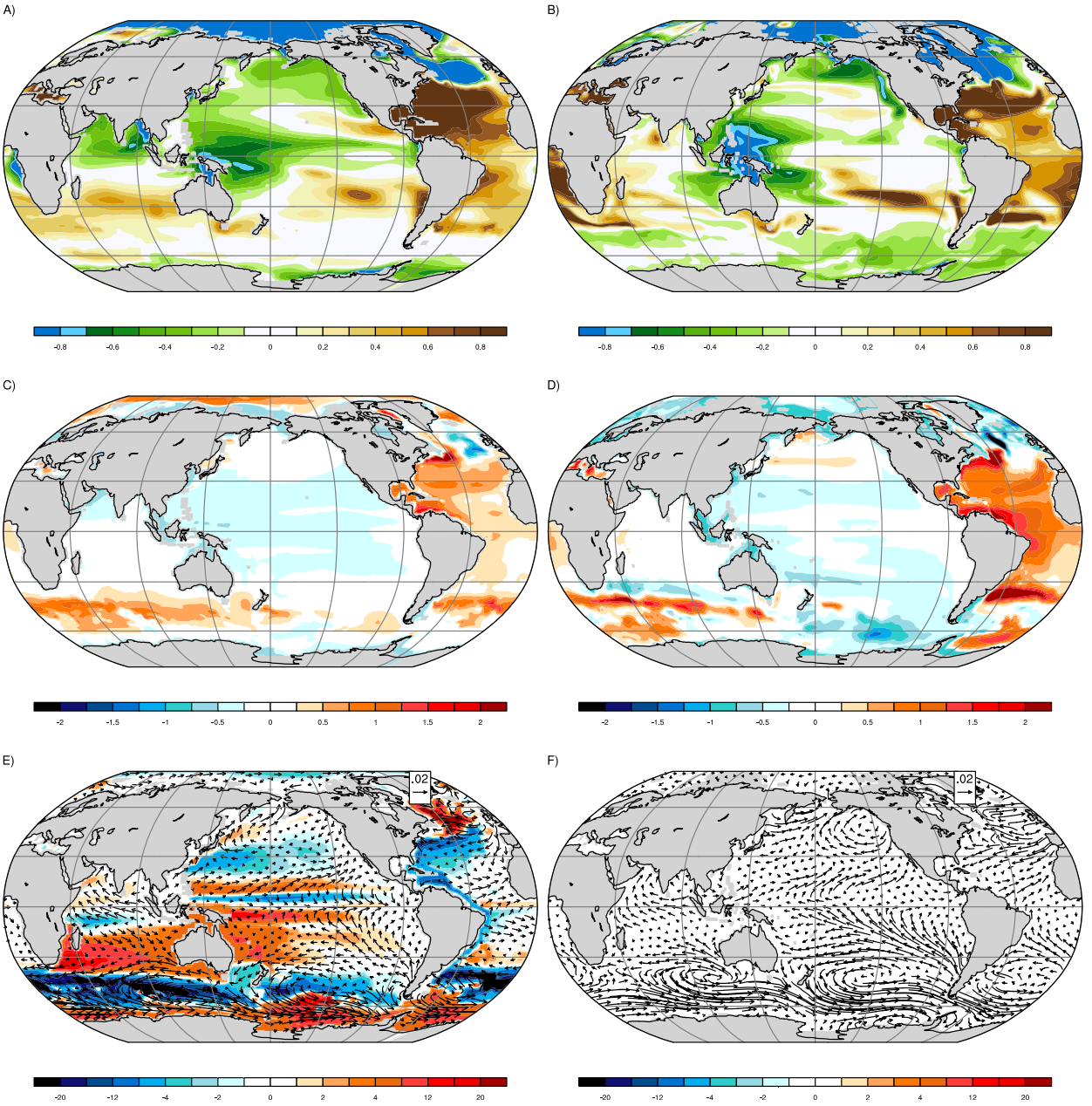

FIG. 7. Trends in (a),(b) SSS (psu century^{-1}), (c),(d) full-depth OHC (10^8 J century^{-1}), and (e),(f) the barotropic streamfunction (BSF; Sv century^{-1}; 1 Sv $\equiv 10^6$ m^3 s^{-1}) and surface stresses [N m^{-2} century^{-1}, reference vector = 0.02 in (e) at top right]. (left) CESM LE from 1920 to 2100 and (right) GFDL LE from 1950 to 2100. BSF is not available for the GFDL LE.The color legend in (a),(b) runs from −0.8 to 0.8 in increments of 0.2; for (c),(d) from −2 to 2 increments of 0.5; and (e),(f) from −20 to 20 in increments of 2.

North Atlantic, with SSH rising sharply north of the Gulf Stream and falling south of it. The North Pacific is not affected by changes in the MOC, so there the SSH falls to the north of the Kuroshio and rises to the south, which is due to a strengthening of the subpolar gyre in response to a deepening Aleutian low. The difference in the South Atlantic regressions between the CESM and GFDL models is most likely due to the different SSS trends shown in Figs. 7a,b. Yin et al. (2010) conclude that the SSH changes in the Southern Ocean are mainly forced by the strengthening and poleward shift of the Southern Hemisphere westerlies, which drive circulation changes in the location of the ACC.

Figures 8a,b show the AC regression between OHC and SSH in the CESM 1850 control and LE runs. The annual cycles are very similar and show positive

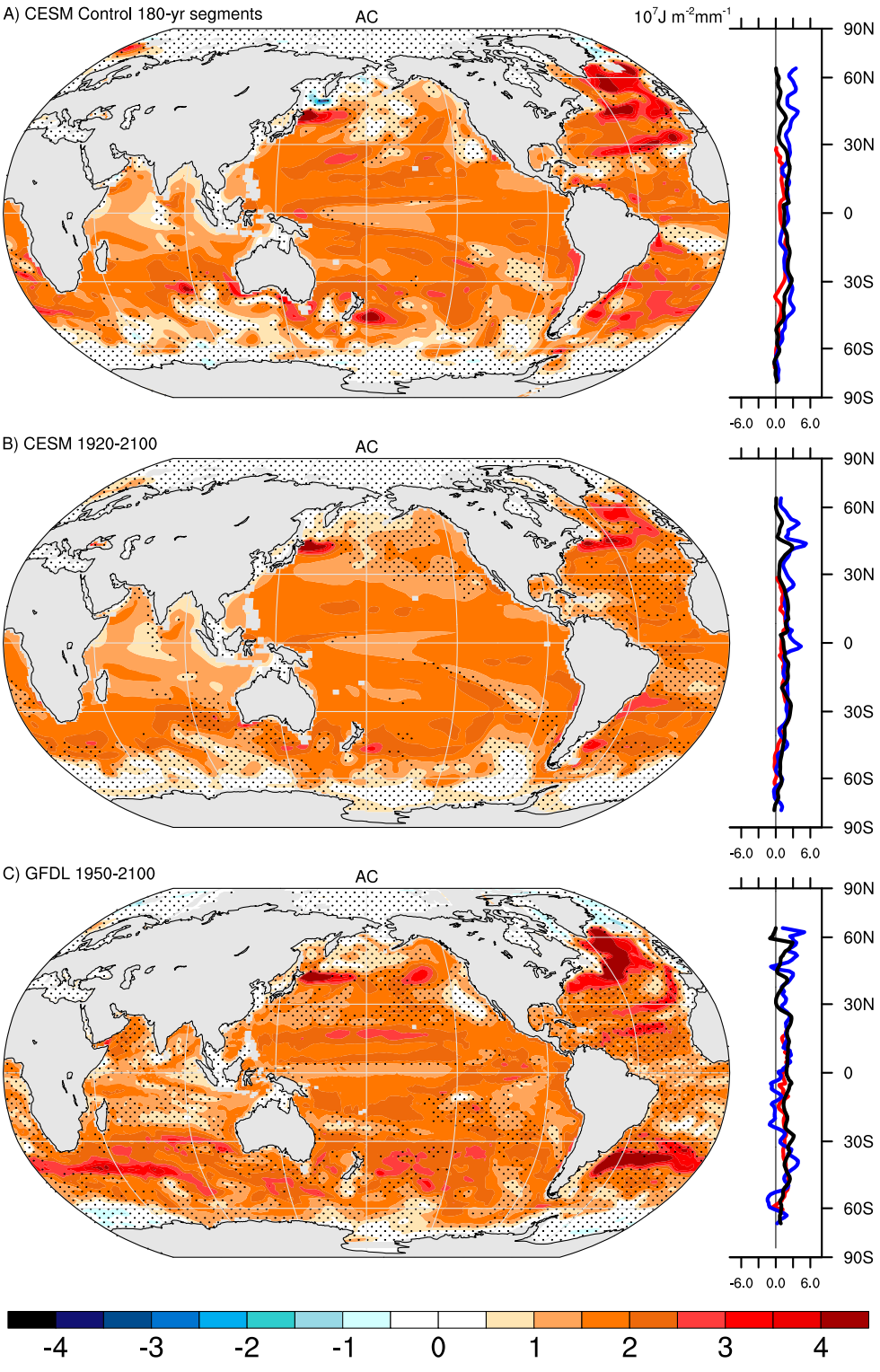

FIG. 8. As in Fig. 6, but for the mean annual cycle.

regressions everywhere except in the Arctic and Southern Ocean near Antarctica. Note that these regions are stippled, indicating that OHC explains less than half the SSH variance. This implies that changes in OHC drive the annual cycle in SSH, except where the annual cycle in ocean circulation dominates the SSH budget. However, there are differences in that the LE regression is smaller in the subpolar and subtropical North Atlantic, and these regions are stippled. This is an indication that the annual cycle has changed late in the twenty-first century under the strong RCP8.5 forcing relative to the altimeter era (Fig. 4b). Comparison of Figs. 8b and 8c shows that the AC regressions in the CESM and GFDL LE have differences in that the amplitude of the GFDL regression is larger than in the CESM. Again the largest differences between CESM and GFDL are in the Atlantic Ocean, where changes in SSS probably produce the small negative regressions in the GFDL model. The different annual cycles explain some differences between the ALL frequency regressions in Figs. 6b,c. Nonetheless, there is some model dependence in the OHC–SSH relationship, even for the annual cycle.

Figure 9 is similar to Fig. 6 but for the HIGH regressions. It shows there is very little difference between the regressions and stippled regions in the CESM LE forced and control runs, and high-frequency relationships are the most consistent both between models and observations (Figs. 3c and 4c) and between models (Figs. 9b,c). It is on this time scale therefore that OHC inferences from SSH are likely to be most reliable. Yet there are some differences between the CESM and GFDL LEs in that the GFDL regression is again larger than the CESM, especially in the Atlantic Ocean, where there is also much more extensive stippling. However, the regions where the regressions are positive and negative are consistent between the models, with negative regressions off Antarctica and in the Arctic Ocean. The reason for the consistency is that SSH across the ACC is mostly set by ocean circulation and in the Arctic it is set by variations in density due to salinity rather than temperature. Thus, intermodel contrasts in ocean dynamics are the most likely contributor to the OHC–SSH high-frequency regression differences, yet these are generally small relative to other model dependencies, such as the water cycle for example.

Figure 10 is similar to Fig. 6 but for LOW-frequency regressions. Here there are very large differences between the CESM control and LE runs (note that the control-run-mapped values in Fig. 10a have been multiplied by a factor of 2 for plotting purposes). The reason is that there are large changes to the base-state climate in LE runs but not in the control run. The regression in the control run is positive nearly everywhere, except in the Arctic Ocean, and is quite similar to the HIGH-frequency regression (Fig. 9a). This shows that OHC variability is the main source of SSH variability when the climate is not subject to strong external forcing. Figures 10b,c show this is definitely not the case in the full-length forced LE runs, where the regression is strongly negative in much of the North Atlantic, midlatitude Pacific, and Indian Oceans and near Antarctica in both the CESM and GFDL LEs. These regions are stippled, indicating that OHC explains less than half the SSH variance. Despite these shared features, there are considerable differences between the CESM and GFDL regressions in the Atlantic and northwest Indian Oceans, which are therefore highlighted as regions of particularly large uncertainty in the LOW-frequency SSH–OHC relationship.

Relating these differences to simulated trends (Fig. 7), the SSS trends in the Pacific are quite similar in the CESM and GFDL LE, but there are substantial differences in the Atlantic and Indian Oceans. The pattern of SSS trends in the Atlantic and Indian Oceans explains key aspects of the differences in the low-frequency regressions in those regions seen in Figs. 10b,c. There is stronger freshening in the Southern Ocean in the GFDL LE than in the CESM, but the low-frequency regressions are similar there. The regressions are also similar in the high North Pacific, which Yin et al. (2010) show is caused by a change in the strength of the subpolar gyre. In summary, the CESM and GFDL LOW negative regressions are quite similar in regions where the OHC–SSH relationship is overwhelmed by changes in the ocean circulation, but they are rather different in regions where changes in SSS are dominant. It is again notable that the LOW regressions from observations (Fig. 3d) also have negative regressions in the southern Indian Ocean and near Antarctica. Figure 10 shows that the LOW regressions between OHC and SSH are rather complicated in both models in LE runs over the twenty-first century when the climate is undergoing substantial transient change due to the strong RCP8.5 forcing scenario. The water cycle between the atmosphere and ocean is enhanced by the warmer climate leading to trends in SSS and the ocean circulation changes in response to altered atmospheric surface winds. The observed negative regressions in these regions suggest the emerging influence of such processes also likely complicates direct inferences between OHC and SSH variability on low frequencies during the altimeter record.

To test the robustness of the model regressions, the CESM regressions were applied to the GFDL model results over the altimeter period of 1993–2015. All four regressions were calculated from the 40-member CESM ensemble and applied to all 30 members of the GFDL

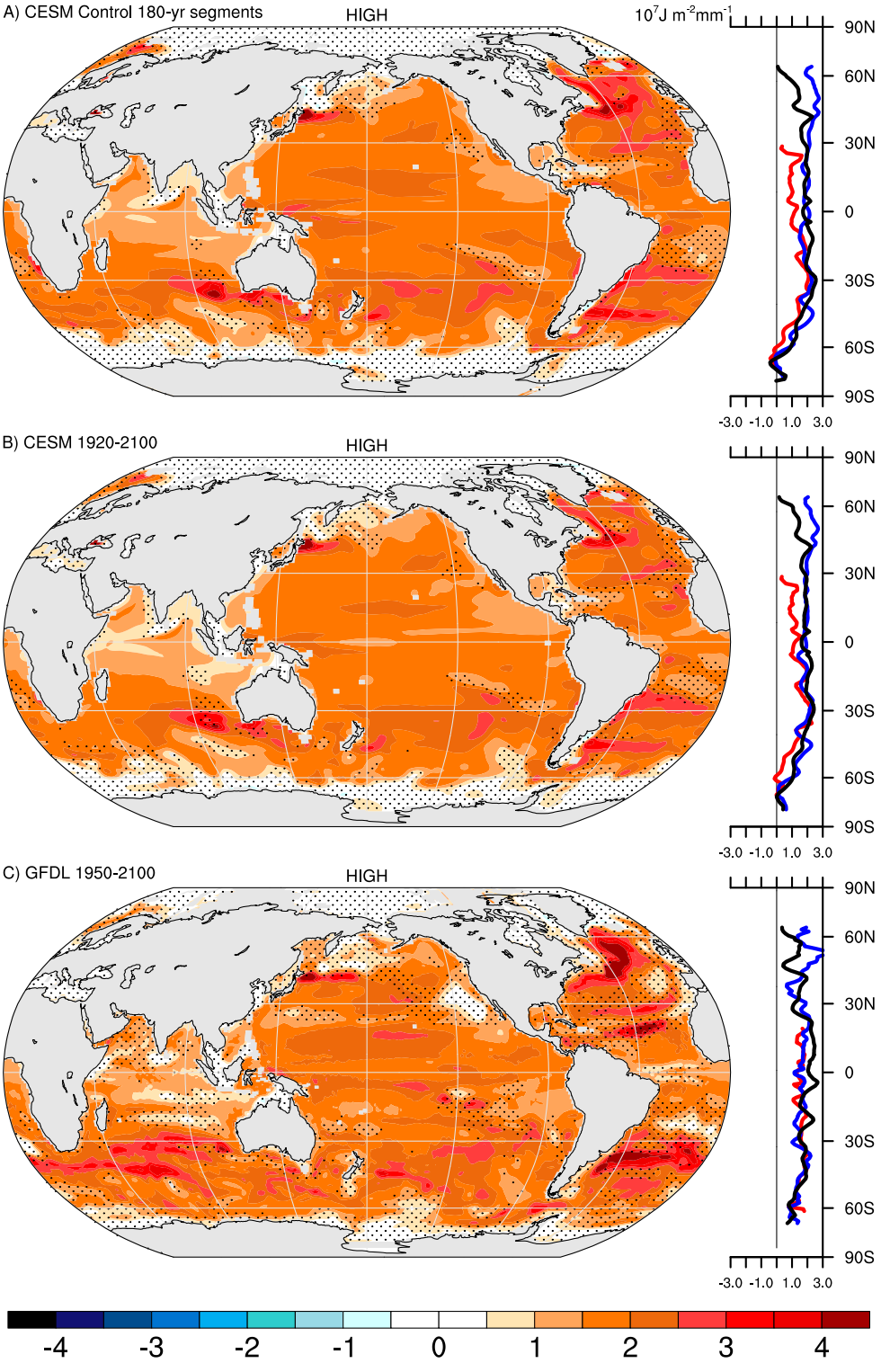

FIG. 9. As in Fig. 6, but for HIGH frequencies.

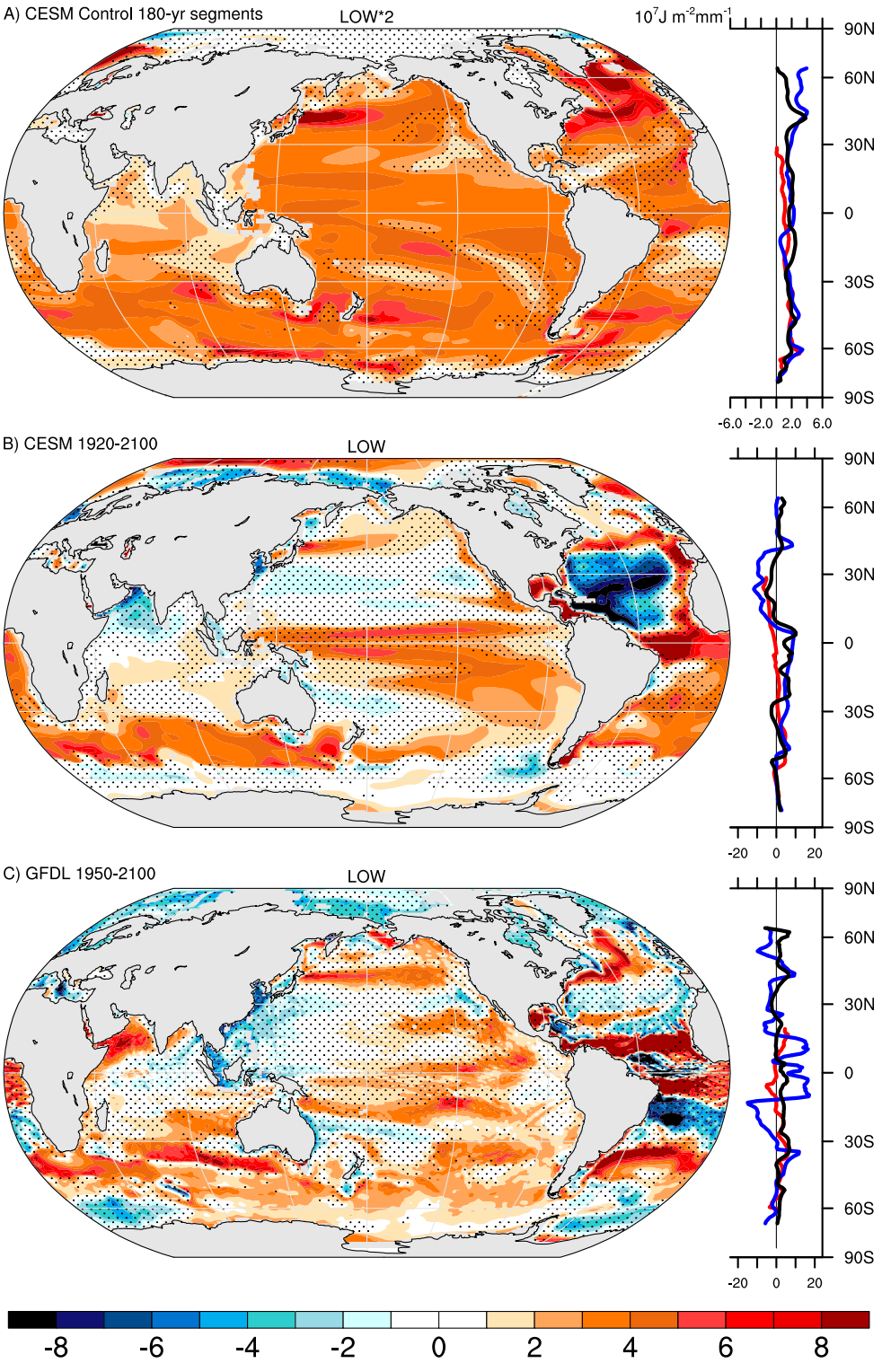

FIG. 10. As in Fig. 6, but for LOW frequencies. Note that the control run values in (a) have been multiplied by a factor of 2.

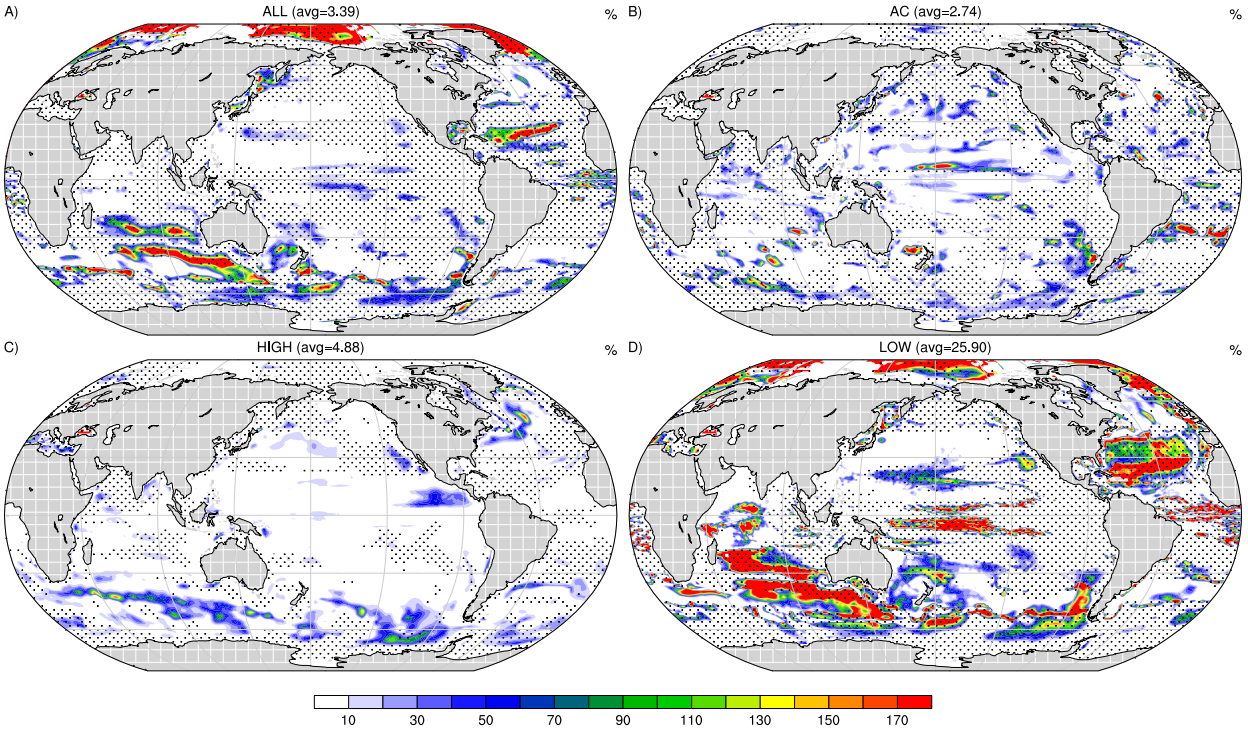

FIG. 11. Percentage increase in the root-mean-square error between the fit to OHC over 1993–2015 using the CESM regressions in the GFDL model: (a) ALL, (b) AC, (c) HIGH, and (d) LOW time-scale filtering.

ensemble. Figure 11 shows the percentage increase in the root-mean-square (rms) error between the fit to OHC using the CESM regressions in the GFDL model as compared to using the GFDL regressions. The stippled regions are taken from the GFDL results in Figs. 6 and 8–10. Figure 11c shows there is <10% increase in rms error over much of the oceans for the HIGH regression, with significant increases only in the Gulf Stream and ACC. For the AC regression, there are a few small regions where the rms error is increased significantly (Fig. 11b) but much more extensive regions where the LOW regression rms error is increased significantly (Fig. 11d). The LOW regression increases are in the Arctic, North Atlantic, south Indian, and Southern Oceans, with smaller regions in the tropical Pacific and Atlantic Oceans. The large rms error increases in the LOW regression show up in the ALL regression (Fig. 11a). Figure 11 shows that the AC and HIGH regressions are largely robust between the CESM and GFDL results, but the LOW regression is not robust over significant regions of the oceans, due to the different SSS and ocean circulation responses under long-term climate change.

5. Discussion and conclusions

Ultimately, the use of altimetry as an effective constraint on OHC, transports, and surface fluxes will depend on the temporal and spatial scales involved. At HIGH-frequency time scales, a strong and robust relationship between OHC and SSH exists in most regions, which is consistent across observations and models (Figs. 3c, 4c, 5c, and 11c). These relationships could be useful in inferring OHC changes from SSH, as direct observations and reanalyses of OHC often contain a sizeable contribution from noise related to sampling deficiencies at high frequencies (Trenberth et al. 2016). The AC regressions between observations and models (Figs. 3b, 4b, 5b, and 11b) are not quite as robust as for HIGH frequencies, but strong relationships exist at mid- and low latitudes. However, the LOW-frequency regressions over 1993–2015 (Figs. 3d, 4d, 5d, and 11d) show significant regions where OHC explains less than half the SSH variance and where the observed, CESM, and GFDL regressions show considerable differences. On these longer time scales and in smaller ocean regions, where salinity and dynamical ocean effects dominate, direct inferences between OHC and SSH are particularly uncertain. However the regions where ORAP5 depicts anomalous OHC increases during the recent hiatus, such as the Indian and western Pacific Ocean, are regions where both the CESM and GFDL models exhibit modest to strong regressions from 1993–2015 (Figs. 4d and 5d). Therefore, altimetry is also suggestive of anomalous warming in these regions. However,

LOW-frequency regressions are not robust in many other regions and so would contribute substantial uncertainty to inferring OHC from SSH.

Many of these conclusions hold when regressions are calculated from the much longer 1950–2100 CESM and GFDL integrations. The HIGH-frequency (Figs. 9b,c) and AC (Figs. 8b,c) regressions remain robust between the CESM and GFDL models, although there are larger differences compared to those over 1993–2015. However, the LOW-frequency (Figs. 10b,c) regressions become more different over the twenty-first century compared to the altimeter era, especially in the Atlantic Ocean. Comparison of Figs. 3d and 10b,c shows that the LOW regression derived from observations is very different than the low-frequency regressions from long integrations of the climate models. The reason is that the climate has changed very significantly in the LE because of the strong forcing over the twenty-first century, whereas the climate has not changed nearly as much over 1993–2015. Nevertheless, early indications of this influence are suggested in the LOW-frequency regressions in observations (Fig. 3d).

Given these conclusions, it remains an open question for future work as to whether methods can be implemented with sufficient accuracy to infer OHC changes on a global scale during 1993–2005, which is when there were SSH observations but very few OHC observations. The similarity of the regressions from observations and the CESM (Figs. 3a and 4a) holds some promise that this can be done. It would require knowledge of the changes in global SSS and ocean circulation, such as the ACC and Atlantic MOC, during the 1993–2005 period or an understanding of how complementary fields (e.g., surface winds and currents) relate to these fields. These changes could be taken from a model, but it would be better to use the changes in the real ocean. Unfortunately, these quantities were not well measured during 1993–2005. Development of a method to infer OHC, guided by observed variability during the Argo era and climate models, holds the promise of extending a detailed understanding of OHC variability back to the beginning of the altimeter era. This would have major implications not only for the understanding of SSH but of broader climate questions relating to ocean heat uptake variability and efficiency and transient and equilibrium climate sensitivities.

Acknowledgments. Dr. Fasullo's participation was supported through NSF Award AGS-1243107, NASA Award NNH11ZDA001N, and DOE Award DE-SC0012711. NCAR is sponsored by the National Science Foundation. Thanks to an anonymous reviewer who suggested the analysis shown in Fig. 11.

REFERENCES

Chambers, D. P., B. D. Tapley, and R. H. Stewart, 1998: Measuring heat storage changes in the equatorial Pacific: A comparison between TOPEX altimetry and Tropical Atmosphere-Ocean buoys. *J. Geophys. Res.*, **103**, 18 591–18 597, doi:10.1029/98JC01683.

Dunne, J. P., and Coauthors, 2012: GFDL's ESM2 global coupled climate–carbon Earth system models. Part I: Physical formulation and baseline simulation characteristics. *J. Climate*, **25**, 6646–6665, doi:10.1175/JCLI-D-11-00560.1.

Durack, P. J., S. E. Wijffels, and R. J. Matear, 2012: Ocean salinities reveal strong global water cycle intensification during 1950 to 2000. *Science*, **336**, 455–458, doi:10.1126/science.1212222.

——, P. Gleckler, F. W. Landerer, and K. E. Taylor, 2014: Quantifying underestimates of long-term upper-ocean warming. *Nat. Climate Change*, **4**, 999–1005, doi:10.1038/nclimate2389.

England, M. H., and Coauthors, 2014: Recent intensification of wind-driven circulation in the Pacific and the ongoing warming hiatus. *Nat. Climate Change*, **4**, 222–227, doi:10.1038/nclimate2106.

Forget, G., and R. M. Ponte, 2015: The partition of regional sea level variability. *Prog. Oceanogr.*, **137**, 173–195, doi:10.1016/j.pocean.2015.06.002.

Frankcombe, L. M., P. Spence, A. McC. Hogg, M. H. England, and S. M. Griffies, 2013: Sea level changes forced by Southern Ocean winds. *Geophys. Res. Lett.*, **40**, 5710–5715, doi:10.1002/2013GL058104.

Guinehut, S., P.-Y. Le Traon, and G. Larnicol, 2006: What can we learn from global altimetry/hydrography comparisons? *Geophys. Res. Lett.*, **33**, L10604, doi:10.1029/2005GL025551.

IPCC, 2013: *Climate Change 2013: The Physical Science Basis*. Cambridge University Press, 1535 pp.

Jahn, A., and M. M. Holland, 2013: Implications of Arctic sea ice changes for North Atlantic deep convection and the meridional overturning circulation in CCSM4-CMIP5 simulations. *Geophys. Res. Lett.*, **40**, 1206–1211, doi:10.1002/grl.50183.

Jayne, S. R., J. M. Wahr, and F. O. Bryan, 2003: Observing ocean heat content using satellite gravity and altimetry. *J. Geophys. Res.*, **108**, 3031, doi:10.1029/2002JC001619.

Kay, J. E., and Coauthors, 2015: The Community Earth System Model (CESM) large ensemble project: A community resource for studying climate change in the presence of internal climate variability. *Bull. Amer. Meteor. Soc.*, **96**, 1333–1349, doi:10.1175/BAMS-D-13-00255.1.

Knutti, R., D. Masson, and A. Gettelman, 2013: Climate model genealogy: Generation CMIP5 and how we got there. *Geophys. Res. Lett.*, **40**, 1194–1199, doi:10.1002/grl.50256.

Köhl, A., 2014: Detecting processes contributing to interannual halosteric and thermosteric sea level variability. *J. Climate*, **27**, 2417–2426, doi:10.1175/JCLI-D-13-00412.1.

Meehl, G. A., J. M. Arblaster, J. T. Fasullo, A. Hu, and K. E. Trenberth, 2011: Model-based evidence of deep-ocean heat uptake during surface-temperature hiatus periods. *Nat. Climate Change*, **1**, 360–364, doi:10.1038/nclimate1229.

——, and Coauthors, 2013: Climate change projections in CESM1(CAM5) compared to CCSM4. *J. Climate*, **26**, 6287–6308, doi:10.1175/JCLI-D-12-00572.1.

Meijers, A. J. S., E. Shuckburgh, N. Bruneau, J.-B. Sallee, T. J. Bracegirdle, and Z. Wang, 2012: Representation of the Antarctic Circumpolar Current in the CMIP5 climate models and

future changes under warming scenarios. *J. Geophys. Res.*, **117**, C12008, doi:10.1029/2012JC008412.

Mitrovica, J. X., M. E. Tamisiea, J. L. Davis, and G. A. Milne, 2001: Recent mass balance of polar ice sheets inferred from patterns of global sea-level change. *Nature*, **409**, 1026–1029, doi:10.1038/35059054.

Nerem, R. S., D. P. Chambers, C. Choe, and G. T. Mitchum, 2010: Estimating mean sea level change from the TOPEX and Jason altimeter missions. *Mar. Geod.*, **33**, 435–446, doi:10.1080/01490419.2010.491031.

Pardaens, A. K., J. M. Gregory, and J. A. Lowe, 2011: A model study of factors influencing projected changes in regional sea level over the twenty-first century. *Climate Dyn.*, **36**, 2015–2033, doi:10.1007/s00382-009-0738-x.

Rodgers, K. B., J. Lin, and T. L. Frölicher, 2015: Emergence of multiple ocean ecosystem drivers in a large ensemble suite with an Earth system model. *Biogeosciences*, **12**, 3301–3320, doi:10.5194/bg-12-3301-2015.

Roemmich, D., and J. Gilson, 2009: The 2004–2008 mean and annual cycle of temperature, salinity, and steric height in the global ocean from the Argo program. *Prog. Oceanogr.*, **82**, 81–100, doi:10.1016/j.pocean.2009.03.004.

Sato, O. T., P. S. Polito, and W. T. Liu, 2000: Importance of salinity measurements in the heat storage estimation from TOPEX/POSEIDON. *Geophys. Res. Lett.*, **27**, 549–551, doi:10.1029/1999GL011003.

Smith, R., and Coauthors, 2010: The Parallel Ocean Program (POP) reference manual: Ocean component of the Community Climate System Model (CCSM) and Community Earth System Model (CESM). Los Alamos National Laboratory Tech. Rep. LAUR-10-01853, 141 pp., http://ccsm.ucar.edu/models/cesm1.1/pop2/doc/sci/POPRefManual.pdf.

Suzuki, T., and M. Ishii, 2011: Long-term regional sea level changes due to variations in water mass density during the period 1981–2007. *Geophys. Res. Lett.*, **38**, L21604, doi:10.1029/2011GL049326.

Swart, N. C., and J. C. Fyfe, 2012: Observed and simulated changes in the Southern Hemisphere surface westerly wind-stress. *Geophys. Res. Lett.*, **39**, L16711, doi:10.1029/2012GL052810.

Trenberth, K. E., and J. T. Fasullo, 2013: An apparent hiatus in global warming? *Earth's Future*, **1**, 19–32, doi:10.1002/2013EF000165.

——, and Coauthors, 2007: Observations: Surface and atmospheric climate change. *Climate Change 2007: The Physical Science Basis*, S. Solomon et al., Eds., Cambridge University Press, 235–336.

——, J. T. Fasullo, and J. T. Kiehl, 2009: Earth's global energy budget. *Bull. Amer. Meteor. Soc.*, **90**, 311–323, doi:10.1175/2008BAMS2634.1.

——, ——, K. von Schuckmann, and L. Cheng, 2016: Insights into Earth's energy imbalance from multiple sources. *J. Climate*, **29**, 7495–7505, doi:10.1175/JCLI-D-16-0339.1.

van Vuuren, D., and Coauthors, 2011: The representative concentration pathways: An overview. *Climatic Change*, **109**, 5–31, doi:10.1007/s10584-011-0148-z.

Vinogradova, N. T., and R. M. Ponte, 2013: Clarifying the link between surface salinity and freshwater fluxes on monthly to interannual time scales. *J. Geophys. Res. Oceans*, **118**, 3190–3201, doi:10.1002/jgrc.20200.

White, W. B., and C.-K. Tai, 1995: Inferring interannual changes in global upper ocean heat storage from TOPEX altimetry. *J. Geophys. Res.*, **100**, 24 943–24 954, doi:10.1029/95JC02332.

Yin, J., S. M. Griffies, and R. J. Stouffer, 2010: Spatial variability of sea level rise in twenty-first century projections. *J. Climate*, **23**, 4585–4607, doi:10.1175/2010JCLI3533.1.

Zhang, X., J. A. Church, S. M. Platten, and D. Monselesan, 2014: Projection of subtropical gyre circulation and associated sea level changes in the Pacific based on CMIP3 climate models. *Climate Dyn.*, **43**, 131–144, doi:10.1007/s00382-013-1902-x.

Zuo, H., M. A. Balmaseda, and K. Mogensen, 2015: The new eddy-permitting ORAP5 ocean reanalysis: Description, evaluation and uncertainties in climate signals. *Climate Dyn.*, **49**, 791–811, doi:10.1007/s00382-015-2675-1.